⌘ *Author's Choice*

THE JOURNAL OF BIOLOGICAL CHEMISTRY VOL. 283, NO. 34, pp. 23305–23314, August 22, 2008

Structure of the Human 26S Proteasome

*SUBUNIT RADIAL DISPLACEMENTS OPEN THE GATE INTO THE PROTEOLYTIC CORE**

Received for publication, April 8, 2008 Published, JBC Papers in Press, June 5, 2008, DOI 10.1074/jbc.M802716200

Paula C. A. da Fonseca and Edward P. Morris[1]

From the Section of Structural Biology, The Institute of Cancer Research, London SW3 6JB, United Kingcom

The 26S proteasome plays an essential role in regulating many cellular processes by the degradation of proteins targeted for breakdown by ubiquitin conjugation. The 26S complex is formed from the 20S core, which contains the proteolytic active sites, and 19S regulatory complexes, which bind to the 20S core to activate it and confer specificity for ubiquitinated protein substrates. We have determined the structure of the human 26S proteasome by electron microscopy and single particle analysis. In our reconstructions the crystallographic structure of each of the subunits of the 20S core can be unambiguously docked by direct recognition of each of their densities. Our results show for the first time that binding of the 19S regulatory particle results in the radial displacement of the adjacent subunits of the 20S core leading to opening of a wide channel into the proteolytic chamber. The analysis of a proteasome complex formed from one 20S core with a single 19S regulatory particle attached serve as control to our observations. We suggest locations for some of the 19S regulatory particle subunits.

The eukaryotic 26S proteasome is a multisubunit protein complex responsible for controlled degradation of a wide range of targeted intracellular proteins (1), typically labeled by the covalent attachment of a Lys-48 linked poly ubiquitin chain. It has a particularly significant role in cell cycle regulation and apoptosis. The 26S proteasome is composed of a 20S proteolytic core particle (20S-CP)[2] associated with 19S regulatory particles (19S-RPs). Although purified proteasome samples that target polyubiquitinated substrates are generally called 26S proteasome preparations, these are commonly mixtures of 20S-CP particles associated with one or two 19S-RPs (sedimentation coefficients of 26S and 30S, respectively).

X-ray crystallographic studies show that the 20S-CP has a barrel-like structure made up of four stacked heptameric rings (2). In eukaryotes the outer rings are each formed from seven highly homologous subunits, α1–7, whereas the two inner rings are each formed from seven highly homologous subunits, β1–7, with a molecular 2-fold axis located at the interface between the two β rings. The β rings form a central chamber in which proteolysis is catalyzed by the N-terminal Thr residues of β1, β2, and β5 (3). Substrate translocation into this proteolytic chamber takes place via a narrow axial channel in the α rings that admits only peptides and unfolded proteins (4). Although the eukaryotic 20S-CP contains the catalytic sites for proteolysis, it only becomes fully active upon binding of regulatory complexes (5). The 19S-RP is itself made up of two subcomplexes, base and lid (6), which together consist of at least 18 individual subunits responsible for specific polyubiquitinated substrate recognition, de-ubiquination, unfolding, and translocation into the proteolytic core. ATP dependence of the 26S proteasome is associated with six homologous but distinct AAA-ATPase subunits, Rpt1–6, located in the base subcomplex adjacent to the α ring of the 20S-CP (6). Three further subunits, Rpn1, Rpn2, and Rpn10, are also assigned to the base of the 19S-RP, whereas the remaining subunits make up the lid.

Here we describe the three-dimensional structure of the human 26S proteasome, doubly capped with 19S-RPs, determined by single particle analysis of electron microscopy images. In the resulting structure we can unambiguously dock the 20S-CP crystallographic structure, which allowed us to directly observe, for the first time, a novel mechanism by which the binding of 19S-RPs opens the gate into the proteolytic core by subunit displacement within the 20S-CP. A parallel analysis of human single-capped 26S proteasome complexes confirmed our observations.

EXPERIMENTAL PROCEDURES

Electron Microscopy—Samples of human 26S proteasome were obtained from Biomol International, Exeter, UK. The samples were diluted in 50 mM Tris-HCl, pH 7.5, 5 mM $MgCl_2$, 1 mM dithiothreitol, and 2 mM ATP to a final concentration of ~0.1 mg/ml, applied to glow-discharged carbon-coated grids, and negatively stained with 2% (w/v) uranyl acetate. Low-dose images (~20 electrons $Å^{-2}$) were recorded on Kodak SO163 film in a JEOL 1200EX electron microscope at 100-kV accelerating voltage and at a calibrated magnification of 35,000×.

Image Analysis, Three-dimensional Reconstruction, and Coordinate Docking—Electron microscopy films were digitized using a Nikon 9000 ED Coolscan film scanner at a step size of 6.35 μm to produce 16-bit gray scale images. The images were resampled by averaging patches of 3 × 3 pixels to give a final sampling of 5.44 Å/pixel at the specimen level. As a preliminary step in image processing, data sets of molecular images of proteasome complexes were subjected to automated alignment and classification procedures using the EMAN refine2d program (7). Subsequently to this preliminary evaluation, all image analysis and further processing was carried out using a combination of Imagic (8) and Spider (9) programs. Three-dimen-

* This work was funded by a Project Grant from Cancer Research UK. The costs of publication of this article were defrayed in part by the payment of page charges. This article must therefore be hereby marked "*advertisement*" in accordance with 18 U.S.C. Section 1734 solely to indicate this fact.

[1] To whom correspondence should be addressed: Section of Structural Biology, The Institute of Cancer Research, Chester Beatty Laboratories, 237 Fulham Rd., London, SW3 6JB, UK. E-mail: edward.morris@icr.ac.uk.

[2] The abbreviations used are: 20S-CP, 20S core particle; 19S-RP, 19S regulatory particle.

⌘ *Author's Choice*—Final version full access.

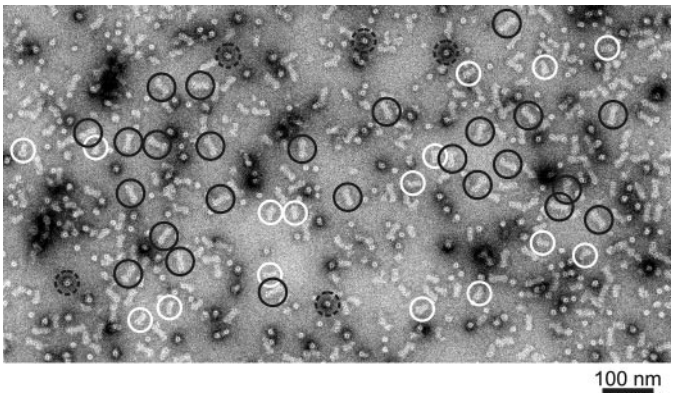

FIGURE 1. **Electron micrograph of a negatively stained 26S proteasome sample.** Examples of side views of double-capped and single-capped 26S proteasome images are identified with *black* and *white circles*, respectively. End views of 26S proteasome complexes are identified by *black dashed circles*.

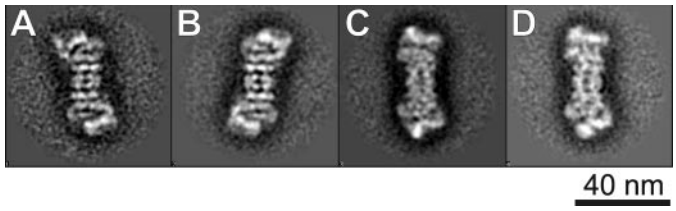

FIGURE 2. **Selection from the initial class averages derived for side views of double-capped 26S proteasomes by automated alignment and classification procedures.** *A* and *B*, class averages with 2-fold rotational symmetry characteristic of a projection along a C2 axis. *C*, class average with mirror symmetry characteristic of a projection normal to a C2 axis. *D*, example of an asymmetric class average, corresponding to intermediate projections to those along (*A* and *B*) and orthogonal (*C*) to the C2 symmetry axis.

sional reconstructions were visualized with Pymol, which was also used for creation of structure diagrams. Automated docking of crystallographic coordinates was performed with the software URO (10).

RESULTS

Creation of Particle Image Data Sets—Electron microscope images of negatively stained human 26S proteasome samples on carbon support film reveal a variety of molecular shapes. Overall the protein molecular images appear to consist predominantly of a mixture of side views with characteristic rod-like shapes together with views with approximately circular profile (Fig. 1). The side views can be recognized by their characteristic shape as a mixture of double-capped and single-capped 26S proteasome complexes present in approximately equal amounts. In the case of the views with circular profile these have a radius consistent with end-on views of proteasome complexes. However, the end views of the 20S-CP, 26S single-capped, and 26S double-capped complexes are all quite similar in appearance and, therefore, are not readily distinguishable. Therefore, to assemble data sets corresponding to molecular species clearly of the same composition, side views only were carefully selected manually to give a data set of 9,823 images of double-capped and a second data set of 10,568 images of single-capped 26S proteasome complexes.

Calculation of a Reference Model and Refinement of the Three-dimensional Structures—The first step in the analysis of the image data set of the double-capped 26S proteasome was to subject it to fully automated rounds of iterative alignment and classification procedures. This provided an unbiased evaluation of the different molecular views present in the data set. A selection of class averages resulting from this preliminary procedure is shown in Fig. 2. Within this selection it is possible to identify molecular projections with 2-fold rotational symmetry (Fig. 2, *A* and *B*) and mirror symmetry (Fig. 2*C*) together with asymmetric image class averages (*e.g.* Fig. 2*D*). The 2-fold and mirror symmetric projections are characteristic of orthogonal views of a three-dimensional object with C2 point group symmetry (*i.e.* 2-fold rotational symmetry), which is the known symmetry of the 20S-CP and, therefore, the expected symmetry of the double-capped 26S proteasome, assuming both 19S-RP have the same conformation in the complex. In this context asymmetric class averages would correspond to intermediate views to those with 2-fold and mirror symmetries. The clear identification of the C2 symmetry provides a frame of reference for the assignment of projection angles, with angles corresponding to rotations of 0°, 90°, and 180° around the long axis of the proteasome being assigned to the symmetric class averages (Fig. 2, *A*, *C*, and *B*, respectively). An initial three-dimensional model was generated with these angular assignments by the exact-filtered back-projection algorithm using C2 symmetry.

The initial three-dimensional model, low pass-filtered to attenuate the intrinsic distortions associated with the use of a very restricted number of molecular views, was used as the starting point for the image analysis. From this starting model progressively refined three-dimensional structures were calculated by successive rounds of multireference alignment, classification by multivariate statistical analysis, angular assignment by projection matching, and back-projection for the calculation of the three-dimensional volumes, exploiting the C2 symmetry of the double-capped 26S proteasome. Forward projections of the three-dimensional maps calculated for each iterative round were used as references for the next round of alignment. For the last few rounds of the refinement procedure a total of 3000 class averages was calculated, of which about 1000 classes were selected for the three-dimensional reconstructions based on their signal-to-noise ratio, overall internal details, and consistency with the corresponding forward projections of the three-dimensional map, which is a direct indication that indeed those classes correspond to different views of the same complex. At this stage of the analysis a number of end views were also included for completeness of the dataset. This involved careful selection from the original micrographs of end views of double-capped 26S proteasomes identified by their agreement with reprojections of the three-dimensional map. The final three-dimensional structure presented here was calculated from 834 class averages. Apart from a small number of end-on-views, these 834 class averages were predominantly side views well distributed around the long axis of the proteasome complex to which projection angles were assigned with a mean value of 7.47° for the tilt about the proteasome short axis. The results from this analysis are illustrated in Fig. 3*A*, which shows examples of the final class averages used in the three-dimensional reconstruction and the corresponding surface representations of the three-dimensional map and forward projections. The resolution of the three-dimensional analysis of the double-

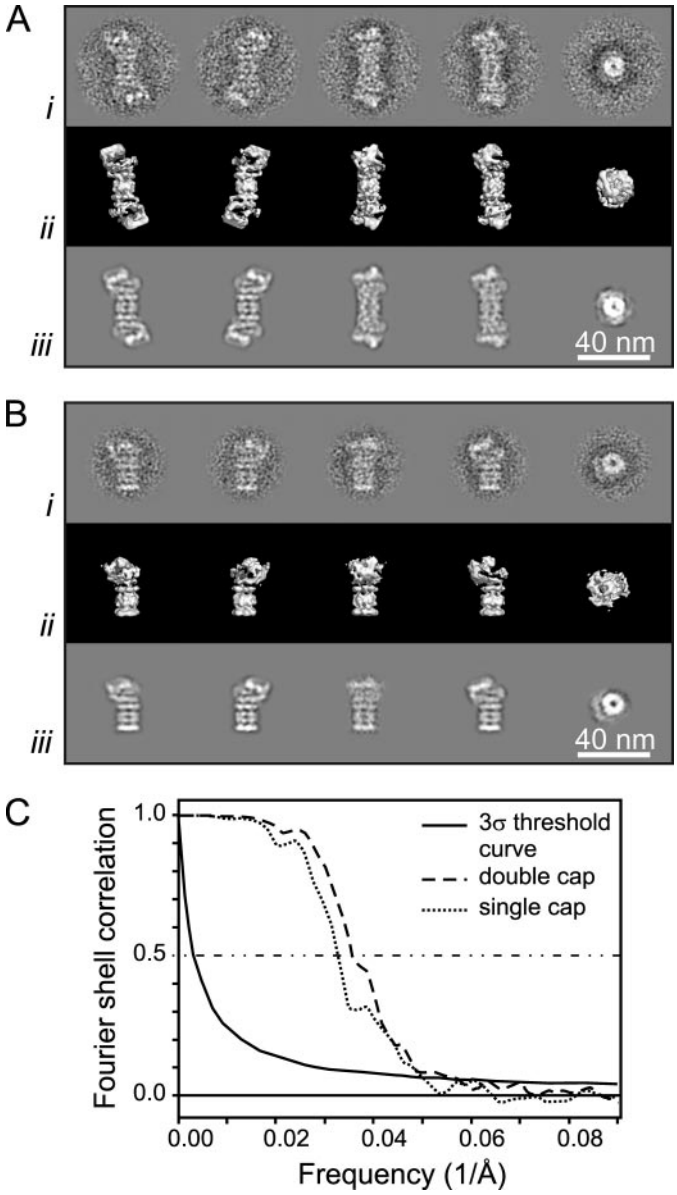

FIGURE 3. **Three-dimensional analysis of the 26S proteasome.** *A*, double-capped 26S proteasome. *B*, single-capped 26S proteasome. *i*, examples of class averages used for three-dimensional reconstruction; *ii*, corresponding surface views of the three-dimensional reconstructions; *iii*, corresponding forward projections of the three-dimensional reconstructions. *C*, resolution assessment by Fourier shell correlation.

capped 26S proteasome estimated from Fourier shell correlation is within 18–28 Å, depending on the resolution criteria considered (Fig. 3*C*). It should be noted that three-dimensional structures determined as presented here can in principle give rise to one of two mirror-related variants that are not readily distinguished in the absence of other information. However, for the current analysis the correct variant (presented here) was unambiguously recognized by its agreement with the crystal structure of the 20S-CP (see below).

The three-dimensional structure of the double-capped 26S proteasome generated as described above was used to produce a reference structure for analysis of the single-capped 26S proteasome data set by removal of the densities corresponding to one of the 19S regulatory particles by appropriate masking followed by re-centering and low pass Fourier filtering of the resulting three-dimensional map. Structural analysis of the single-capped 26S proteasome images was then carried out as described for the double-capped 26S proteasome data but with no symmetry imposed, *i.e.* using C1 point group symmetry. Selected class averages from the 1080 classes contributing to the final three-dimensional map are shown in Fig. 3*B* together with corresponding surface representations of the three-dimensional map and their forward projections. The map of the single-capped 26S proteasome is recognizably noisier than that of the doubly-capped 26S proteasome, which is a consequence of the use of approximately the same number of molecular views but without symmetry imposition. The resolution of the three-dimensional map of the single-capped 26S proteasome estimated from Fourier shell correlation is 20–29 Å (Fig. 3*C*).

Three-dimensional Structures of Double- and Single-capped 26S Proteasomes—The final three-dimensional structures of the 26S proteasomes are illustrated as surface representations in Fig. 4, *panels A* and *B*, respectively. For representation purposes these are contoured to give molecular volumes corresponding to ~2.6 MDa for the double-capped and ~1.7 MDa for the single-capped 26S proteasome maps, assuming a protein density of 0.844 Da $Å^{-3}$. These molecular masses were estimated from the sequence of individual subunits expected to be present in the human 26S proteasome. In both structures the region corresponding to the 20S-CP (Fig. 4, *gray*) is readily identified by its four rings of density and in the 19S-RPs the base and lid regions can also be recognized (*blue*, *magenta*, and *yellow* in Fig. 4). A major feature of the base (Fig. 4, *blue*) is a disc-shaped density adjacent to and approximately parallel with the 20S-CP α ring. Additionally there is an arced density (Fig. 4, *magenta*) that extends from this disc in a tangential direction. The base of the 19S-RP appears connected to the adjacent α ring by three linker densities running parallel to the proteasome long axis (see Fig. 4 and 6, see below). In addition, the double-capped complex is characterized by a prominent L-shaped connection from the base of the 19S-RP to the α ring of the 20S-CP (Figs. 4*A* and 6, see below); in the single-capped complex this density is incompletely recovered (Fig. 4*B*). The lid of the 19S-RP (Fig. 4, *yellow*) consists of a number of apparent subunit densities, and it is approximately of similar size to the base.

Identification of Individual Subunits of the 20S-CP—The quality of our three-dimensional analysis can be assessed by comparing the 20S-CP region of the three-dimensional maps with the corresponding atomic coordinates of its crystal structure (Protein Data Bank code 1IRU) (11). The crystal structure of the 20S-CP is characterized by C2 symmetry (Fig. 5*A*), where a molecular 2-fold symmetry axis relates via a 180° rotation each pair of adjacent α and β rings, which form half of the 20S-CP, with the second α and β pair (2). The same symmetry axis is defined by the C2 symmetry of the double-capped 26S proteasome presented here. Thus, to preserve the common symmetry axis of the 20S-CP and 26S complex, there are only two ways in which the coordinates of the 20S-CP can be docked into the 26S proteasome map. These alternatives correspond to 180° rotations of the 20S-CP coordinates about the long axis of the 26S proteasome, resulting in viewing the 20S-CP along its symmetry axis but from opposite directions. Due to symmetry

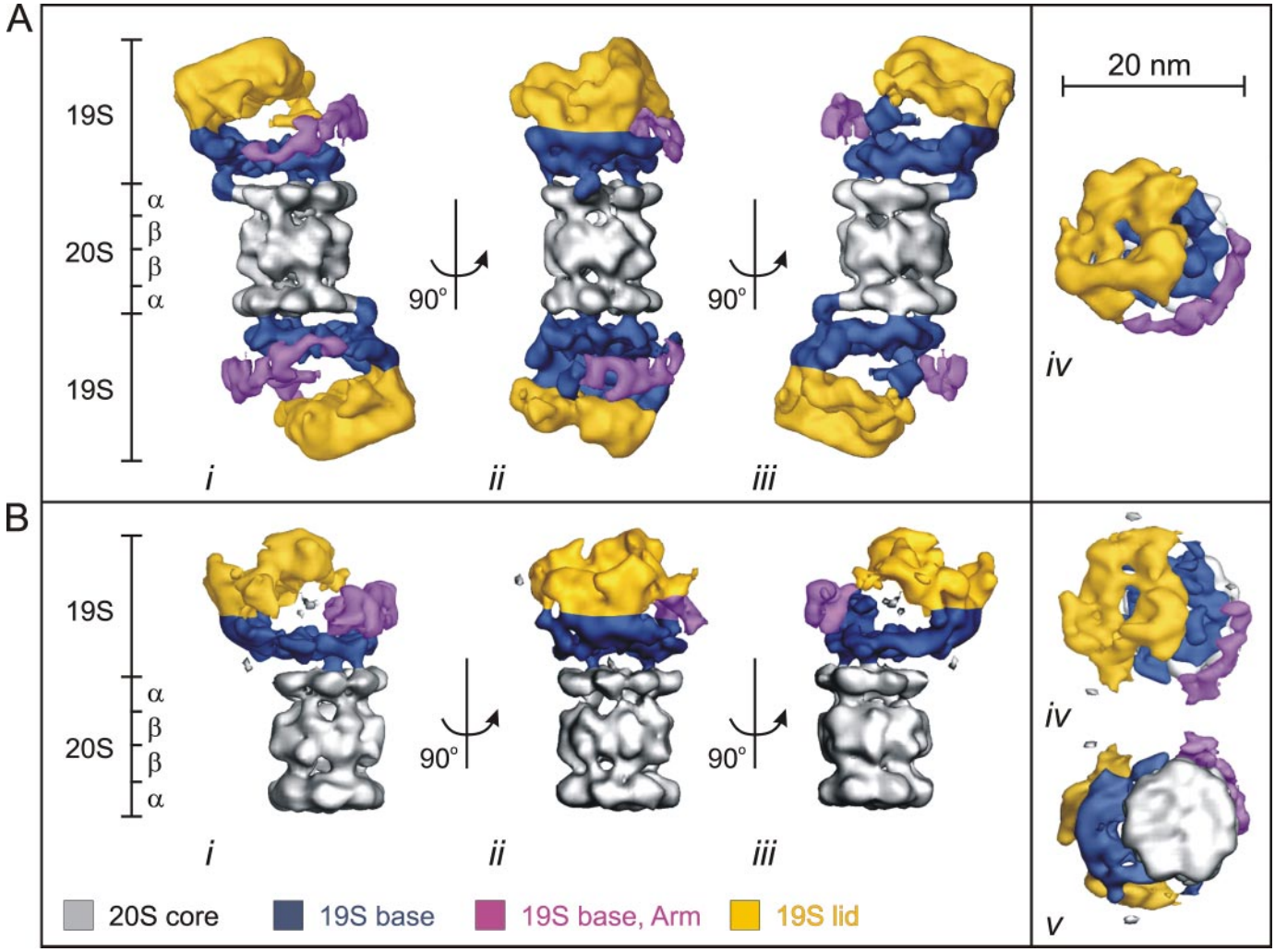

FIGURE 4. **Three-dimensional reconstructions of the 26S proteasome.** *A*, double-capped 26S proteasome. *B*, single-capped 26S proteasome. *i–iii*, side views, with the approximate location of proteasome components indicated (*left*) with viewing directions parallel to the C2 axis (*i*), normal to the C2 axis (*ii*), and parallel to the C2 axis (*iii*), in opposite direction to *i*. *iv*, views from capped ends of the proteasome complexes. *v*, end view from uncapped side of single-capped 26S proteasome.

considerations, any other rotation of the 20S-CP coordinates around the long axis of the 26S proteasome would result in each of the α rings interacting differently with its adjacent 19S-RP. Of the only two possible orientations of the 20S-CP, the correct orientation is clearly identified in our three-dimensional map from the agreement between the individual densities observed for each of the α and β subunits and their counterparts in the crystal structure (Fig. 5, *Bi* and *Ci*). This agreement is not observed if the alternative orientation for the 20S-CP coordinates is taken (Fig. 5*D*), which results in the subunits being systematically located between rather than within the protein density lobes.

The accuracy of the symmetry-based docking was confirmed using the automated docking program URO, which gave near identical results when using the 20S-CP crystal structure as a rigid body. URO fits model electron densities into electron microscope reconstructions using reciprocal space algorithms, thereby avoiding bias introduced when defining the boundaries of the target density (10). The agreement between the densities of our three-dimensional structure and fitted coordinates is particularly apparent in the α subunit rings (Fig. 5*Bi*). The α subunits, although homologous to each other, are characterized by detailed differences in their three-dimensional structure. This is reflected in the three-dimensional map of the double-capped 26S proteasome presented here, where the density corresponding to each α subunit matches its individual molecular envelope (Fig. 5*Bi*). This also provides a clear indication that the handedness of the maps presented here is correct. Docking the 20S-CP coordinates into the single-capped proteasome map, despite its higher level of noise, gives rise to the same orientation to that in the double-capped 26S proteasome and also illustrates good overall agreement between the 20S-CP subunit shapes in the reconstruction and those in the crystal structure (see Fig. 7). This unambiguous docking of the 20S-CP coordinates into the 26S proteasome maps allows, for the first time, the location of each 20S-CP subunit within the 26S complex to be established.

Subunit Rearrangements within the 20S-CP—Despite the good overall agreement between the densities for the 20S-CP in our three-dimensional maps and its x-ray crystallographic structure, close inspection reveals that in our double-capped 26S proteasome reconstruction, the 20S-CP subunits appear to

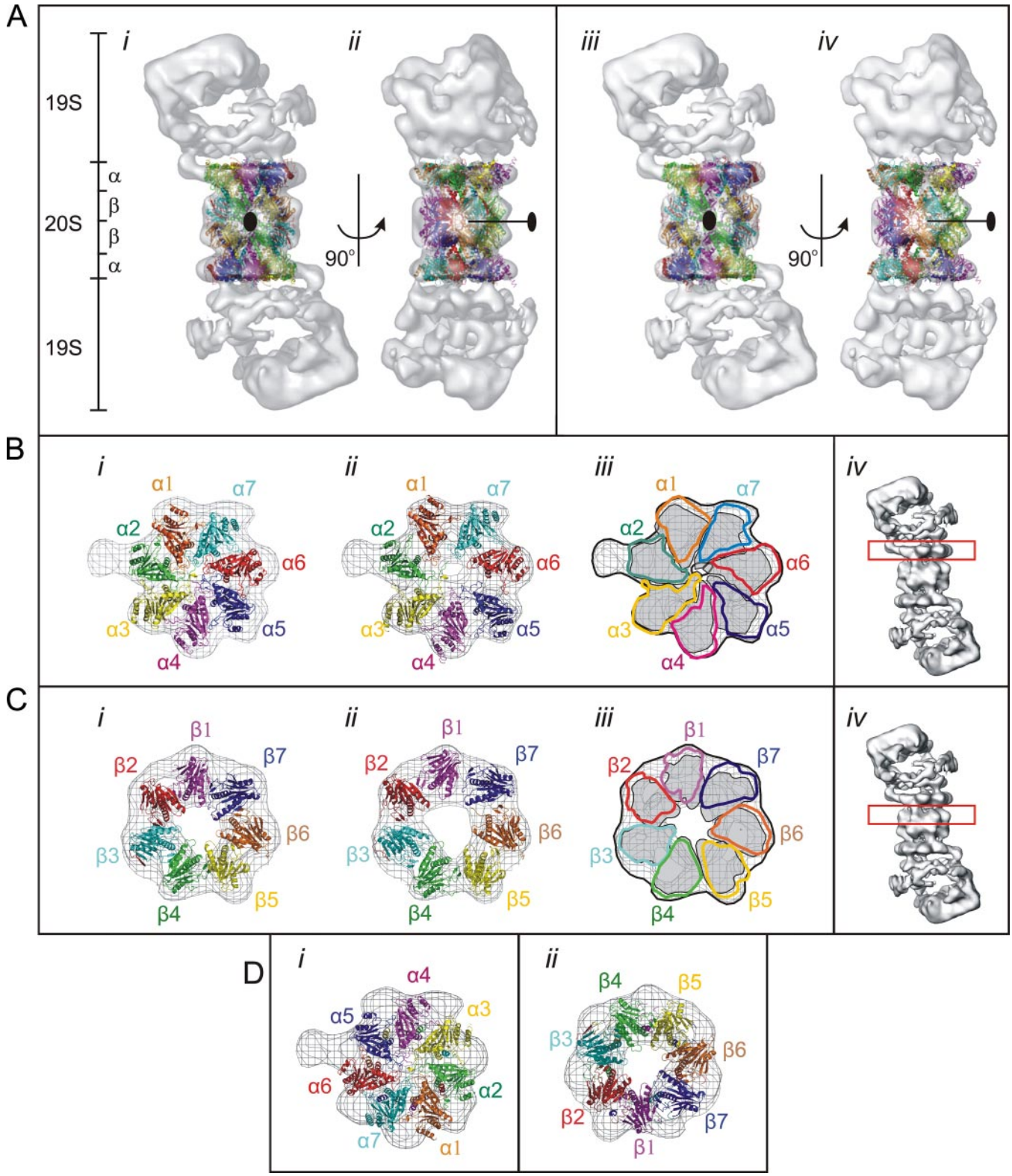

FIGURE 5. **Subunit docking into the 20S-CP region of the double-capped 26S proteasome.** *A*, the crystal structures of the 20S-CP subunits (schematic representation) were docked into the three-dimensional map of the 26S proteasome (transparent surface representation), viewed parallel (*i* and *iii*) and orthogonal (*ii* and *iv*) to the C2 axis shown. The subunits of the 20S-CP were docked as a single rigid body by aligning the common C2 axis (*i* and *ii*) or independently fitted (*iii* and *iv*). The common C2 symmetry axis is represented, and the approximate location of proteasome components is indicated (*left*). *B* and *C*, sections of the 26S proteasome three-dimensional map are shown as *chicken wire*, and crystal structures of docked subunits are represented as *schematics*. *B*, end view of α ring (viewed from 19S-RP). *i*, 20S-CP coordinates docked as a single unit; *ii*, 20S-CP subunits docked independently; *iii*, comparison between *i* (*gray shade*) and *ii* (*colored contours*); *iv*, the section shown in *i–iii* is identified in side view of the 26S proteasome by the *red box*. *C*, end view of β ring (viewed from the adjacent α ring). *Panels i–iv* as for *B*. *D*, sections showing the α and β subunit rings, as for *Bi* and *Ci*, but where the subunits of the 20S core were fitted with a 180° rotation around the proteasome long axis, corresponding to the alternative orientation to that shown in *A*, *B*, and *C*, taking in account the common C2 symmetry axis between the 20S core and the double-capped 26S proteasome. Here the mismatch between the densities of the three-dimensional map and the 20S core crystal structure is apparent.

be at rather higher radius than those in the atomic coordinates; this effect is particularly clear for the α subunits (Fig. 5*Bi*). To assess this observation, the location of the 28 individual subunits of the 20S-CP was investigated by refining the docking of the 20S-CP coordinates with URO software but allowing the coordinates of each individual subunit to be fitted independently, with no symmetry constraints, starting from the 20S-CP crystallographic structure docked as single unit. It should be noted that this fitting procedure depends solely on the densities of the map and is independent of any imposed molecular envelope. The result of this independent docking of the 20S-CP subunits (Fig. 5, *A*, *iii* and *iv*, *Bii*, and *Cii*), although broadly similar to that of the 20S-CP fitted as a single rigid body, matches the molecular envelope of 26S proteasome three-dimensional reconstruction much more closely. Here the most significant movements of the individual 20S-CP subunits correspond to displacements to higher radius than in the crystallographic coordinates (Fig. 5, *Biii* and *Ciii*). The average radial displacement for the α and β subunits is 6 and 5.4 Å, respectively. Although there are also some small lateral displacements and rotations, there are virtually no shifts along the proteasome long axis. This is a clear indication that the displacements observed are real and not just a consequence of inaccurate scaling factors, as these would expand the three-dimensional map in all directions and not just radially. Interestingly, the most substantial radial displacements occur in one segment of the α rings (Fig. 5*Biii*) formed by α1, α4, α5, α6, and α7 (mean radial displacement 7.3 Å), whereas the α2 and α3 subunits are only slightly displaced (mean radial displacement 2.8 Å). Likewise, in the β rings (Fig. 5*Ciii*) a group of 5 subunits, β1, β2, β5, β6, and β7 shows substantially greater radial displacements (mean radial displacement of 6.5 Å) than the remaining two subunits, β3 and β4 (with a mean radial displace-

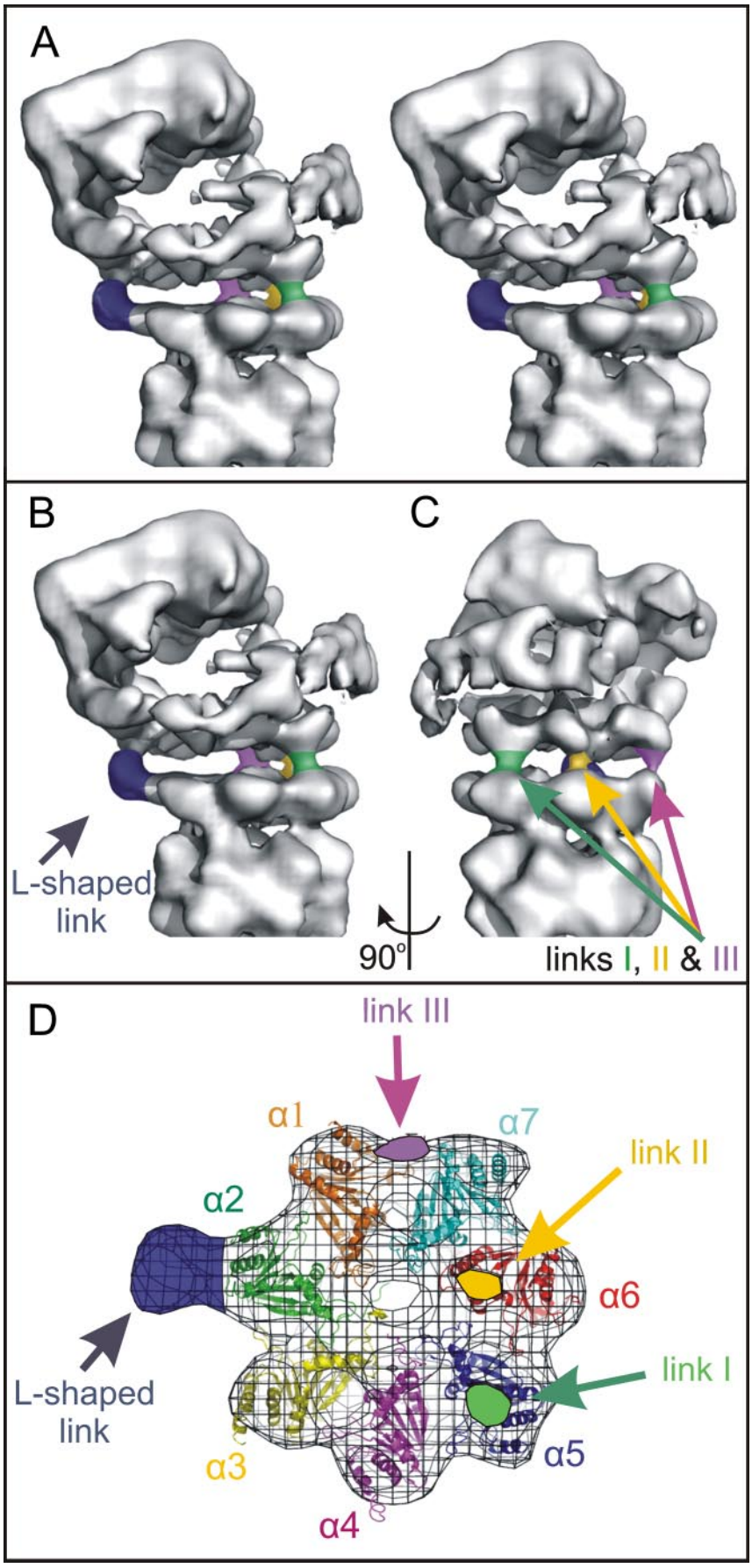

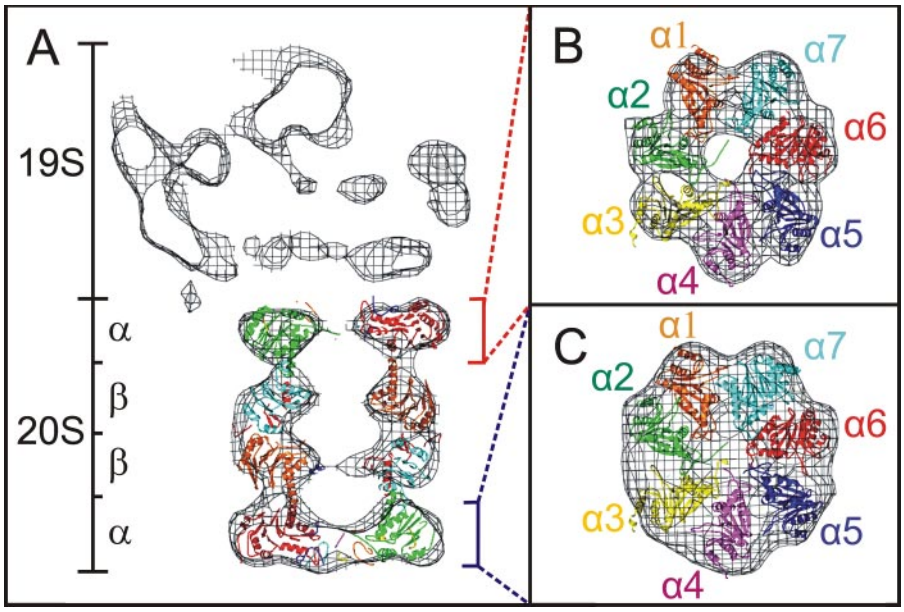

FIGURE 7. **Subunit docking within the 20S-CP of the single-capped 26S proteasome.** Sections of the three-dimensional map are shown as *chicken wire*, and crystal structures of independently docked subunits are represented as *schematics*. *A*, side view, sectioned close to long axis of the proteasome, showing a clear aperture in the α ring adjacent to the 19S-RP. *B*, end view of α ring adjacent to 19S-RP (viewed from the capped end). *C*, end view of α ring at the uncapped end of the 20S-CP (viewed from the free end).

ment of 2.6 Å). The observation that the segments of the α and β rings characterized by larger displacements are overall located on the same side of the 20S-CP suggests that a coordinated subunit rearrangement occurs. These radial displacements appear to leave the 20S-CP subunits still in close contact with their respective neighbors, although the α ring no longer appears to completely enclose the proteolytic core, and an aperture becomes evident near the proteasome long axis (Fig. 5*Bii*). Likewise, radial displacement of the β ring subunits leads to an apparent reduction in the constriction leading to the inner proteolytic chamber (Fig. 5*Cii*). The observation that the segment of the α rings showing the most significant displacements is where the links to the 19S-RP running parallel to the proteasome long axis are bound (Fig. 6, *links I*, *II*, and *III*) indicates a direct association between the binding of the 19S regulatory complex and the 20S-CP subunit rearrangements.

In the single-capped 26S proteasome, it is possible to compare the organization of the 20S-CP subunits located closer to the 19S-RP with those at its uncapped end, allowing us to directly assess the effect of 19S-RP binding on the 20S-CP subunit organization. To this end individual subunits of the 20S-CP were independently docked with URO in the same way as described above for their docking into the double-capped 26S proteasome map. The resulting agreement between the docked 20S-CP subunits and the molecular envelope of the single-capped 26S proteasome reconstruction is apparent (Fig. 7). It is noted that the docked positions for the α subunits in the 20S-CP ring adjacent to the 19S-RP (Fig. 7, *A* and *B*) are very similar to those for the double-capped 26S proteasome (Fig. 5*Bii*), with the formation of an aperture close to the center of this α ring. Remarkably the subunits in the uncapped α ring of the 20S-CP are also displaced to higher radius, but in this case the average radial shift is considerably lower, and the apparent opening of the 20S-CP is not observed (Fig. 7, *A* and *C*). This is in agreement with the corresponding region of the three-dimensional map of the single-capped 26S proteasome, which is characterized by a continuous density (Fig. 4*Bv* and 7, *A* and *C*). The positions of the β subunits after independent docking into the single-capped 26S proteasome map are also characterized by radial shifts compared with those of the 20S-CP crystallographic structure. The average radial displacement observed here was also more significant for the β ring subunits closest to the 19S-RP (average displacement of 7.3 Å) than that for the β ring furthest from the cap (average displacement of 4.7 Å).

DISCUSSION

We describe here the three-dimensional structural analysis by electron microscopy and image processing methods of the human 26S proteasome, where a complex formed by a 20S-CP associated with two 19S-RPs was analyzed exploiting its intrinsic C2 point group symmetry. The level of detail in the final three-dimensional map is sufficient to accurately dock the crystallographic structures of each of the 20S-CP subunits independently. In the resulting structure the α subunits are radially displaced when compared with the crystallographic coordinates of the mammalian 20S-CP (11), revealing a novel mechanism for the opening of a gate into the 20S-CP proteolytic core by the attachment of 19S-RPs. Previous three-dimensional reconstructions and models of *Drosophila* double-capped 26S proteasomes from electron microscopy data have been obtained (12–14), but no functional implications have been described in these previous studies. Overall the three-dimensional maps presented here are in general agreement with the more recent of these structures calculated by cryoelectron tomography (14) and single particle analysis of cryoelectron microscopy images (13).

Subunit Assignment within the Three-dimensional Maps of the Human 26S Proteasome—In the structures of both double- and single-capped human 26S proteasomes described here, the regions corresponding to the 20S-CP and 19S-RPs can be

FIGURE 6. **Links between the 19S-RPs and the 20S-CP of the double-capped 26S proteasome.** *A–C*, side views of three-dimensional map enlarged to show one 19S-RP and approximately half the 20S-CP, with the different links indicated. *A*, stereo representation of view parallel to C2 axis. *B*, view as in *A*, with the L-shaped link indicated. *C*, viewed normal to C2 axis, with *links I*, *II*, and *III* identified. *D*, end view of α ring viewed from 19S-RP with independently docked subunits, as shown in Fig. 5, *Bii*, identifying the attachment sites of the links to the α ring.

readily recognized (Fig. 4). The unambiguous docking of the mammalian 20S-CP crystal structure (11) into our three-dimensional maps allows for the first time the explicit identification of each of the α and β subunits of the 20S-CP within the 26S proteasome (Figs. 5 and 7). In comparison, the absence of high resolution structural data for individual 19S-RP subunits and the current resolution of our three-dimensional analysis impair their definitive assignment. Nevertheless, it is possible to suggest locations for some of those subunits based on information available from earlier studies.

Within the 19S-RP base the disc-like density adjacent to the α ring of the 20S-CP complex (Fig. 4, *blue*) is likely to correspond to the six AAA-ATPase subunits, Rpt1–6, in line with their previously suggested location (6), which is also consistent with that of the archaeal ATPase PAN complex, a homologue of Rpt1–6, when bound to the 20S-CP (15). We found that the 19S-RP base binds the 20S-CP via a prominent L-shaped link which runs between the putative AAA-ATPase densities and the side of the α2 subunit of the 20S-CP (Figs. 4*A* and 6). It is interesting to note that this density is not recovered in the analysis of the single-capped proteasome complex (Fig. 4*B*). However, the fact that in this three-dimensional map the 20S-CP is well defined and that the overall architecture of the 19S-RP remaining densities resemble those in the double-capped complex indicates that the loss of these densities is not a consequence of inaccurate image analysis. It is, therefore, possible to suggest that the subunit corresponding to this L-shaped density may dissociate from the 26S proteasome as a precursor for the full 19S-RP disassembly. In the double-capped 26S proteasome three additional links appear to run parallel to the proteasome long axis, from the putative AAA-ATPase region to the 20S-CP subunits α5 and α6 and the interface between α7 and α1 (Fig. 6, *links I*, *II*, and *III*). The links to α5 and the interface between α7 and α1 are also clearly present in the single-capped proteasome three-dimensional map, although the link to α6 is only partially recovered. Interestingly, a recent study of the effects of Rpt1–6 C-terminal peptides on the mammalian 20S-CP activity suggested that the C terminus of Rpt2, Rpt5, and possibly Rpt1 interact with subunits within the α ring of the 20S-CP and are involved in gate opening and proteasome activation (16). We, therefore, suggest that these three links may correspond to the C-terminal regions of these Rpt subunits.

Apart from the Rpt1–6, the 19S-RP base is also thought to contain the Rpn1, Rpn2, and Rpn10 subunits (6). Rpn1 and Rpn2 are each relatively large (~100 kDa) and sequence analysis by the Phyre server (17) indicates they are substantially composed of armadillo repeats. Armadillo repeats frequently adopt a curved and elongated conformation (18). The arced density (Fig. 4, *magenta*) found at a higher radius to the putative AAA-ATPase region appears to be of appropriate size and shape to correspond to one of these subunits. Both Rpn1 and Rpn2 have been predicted to be made up of curved α/α solenoids (19), although in this earlier work toroidal models were proposed. A higher resolution analysis and specific subunit labeling are required to confirm the assignments proposed here and to establish the full subunit organization within the 19S-RP.

Rearrangements in the 20S-CP α Rings Induced by 19S-RP Binding—The three-dimensional maps of double- and single-capped 26S proteasomes show evidence of rearrangements in the 20S-CP subunits from the crystal structure of the free mammalian 20S-CP. In the single-capped 26S proteasome this rearrangement is most prominent in the α ring adjacent to the 19S-RP (Fig. 7). The positions of individually fitted α subunits, adjacent to 19S-RPs, are characterized by shifts to a higher radius and the creation of a clear open channel close to the central axis of the 20S-CP (Figs. 5*Bii* and 7. A proteasome axial-gated channel has been previously identified as resulting from the rearrangement of N-terminal strands of α2,α3, α4, and α5, without any overall subunit displacement in the crystal structure of 20S-CP in complex with PA26, an 11S regulator (20). The three-dimensional structure of a complex formed between one PA200 cap, another 11 S regulator, and the 20S-CP has also been determined by cryoelectron microscopy and single particle analysis (21). As for the PA26 (20), the PA200 appears to induce the opening of an axial channel within the adjacent α ring without apparent radial displacement of the α subunits. Therefore, the rearrangement we observe in the α rings associated with the attachment of 19S-RPs appears to differ from those induced by 11 S regulators in that it involves not just a local loop reorganization but the radial movement of each of the α subunits, leading to a wider and more prominent channel into the proteolytic core. Such a channel is required for translocation of the target protein substrate, recognized and unfolded by the 19S-RP, into the proteolytic chamber of the 20S-CP. It is interesting to note that from the group of α subunits appearing to be most substantially displaced by the 19S-RP, namely α1, α4, α5, α6, and α7 (Fig. 5*Biii*), the subunits α5, α6, and the interface α1-α7 appear to be joined to the base of the 19S-RP by the links running parallel to the long axis of the proteasome (Fig. 6, *links I*, *II*, and *III*), described above as putative C-terminal ends of Rpt2, Rpt5, and possibly Rpt1 (16). It is, thus, tempting to suggest that these links and, therefore, the association with the 19S-RP, are coupled to the 20S-CP rearrangements associated with channel opening.

The channel in the α rings adjacent to 19S-RPs should function as entry ports into the proteolytic chamber for protein chains unfolded by the 19S-RP and possibly also exit ports for cleaved peptides. The biological role of 11 S regulators is less well established. The 11 S regulators PA28 and PA200 are known to bind to the 20S-CP and activate its proteolysis of model peptides, but they do not recognize ubiquitinated proteins or hydrolyze ATP (22). It has been suggested that the 11 S regulators may form hybrid structures with one 20S-CP and a single 19S-RP (22) and in this context act to create exit ports for cleaved peptides. In this perspective it seems reasonable to suppose that a wider channel, as that shown here induced by 19S-RP binding, would be required for the entry of unfolded proteins compared with that required for exit of cleaved peptides, as originated by 11 S regulator binding. In this light it is interesting to note that Smith *et al.* (16) concluded, from biochemical evidence, that the 20S-CP gate opening mechanisms differ for caps with ATPase subunits, such as the 19S-RP, compared with 11 S regulators.

The three-dimensional map of the single-capped 26S proteasome (Figs. 4*B* and 7) constitutes an internal control to establish if the wider 20S-CP gate opening found in our double-capped proteasome three-dimensional map is indeed a consequence of the 19S-RP binding. Here, the subunit location in the 20S-CP rings adjacent to the 19S-RP can be compared with that at the free side of the 20S-CP (Fig. 7). This analysis revealed that indeed the fitted locations of the α subunits adjacent to the 19S-RP are equivalent to those observed in the double-capped 26S proteasome leading to a substantial aperture close to the 20S-CP central axis. Conversely, fitted positions for the α subunits at the opposite, free end of the 20S-CP are characterized by a significantly reduced radial displacement. In this region of the three-dimensional map there is no apparent axial aperture of the 20S-CP (Fig. 4*Bv* and 7, *A* and *C*). These observations demonstrate that the 20S-CP subunit reorganization observed in our maps indeed results from 19S-RP binding. Furthermore, although it is possible that conformational effects of the binding of a 19S-RP to the 20S-CP may extend to the α ring at the opposite uncapped end of the 20S-CP, any aperture formed at this end is more characteristic of the proposed exit port induced by 11 S regulator binding than the more substantial entry port in 20S-CP α rings bound to 19S-RP.

Rearrangement in the β Subunit Rings—Independent fitting of the 20S subunits into the double- and single-capped 26S proteasome maps led to the β subunits being displaced to higher radius, although to a lesser extent than the α subunits (Fig. 5, *B* and *C*). The β rings of the uncapped 20S-CP form two relatively narrow apertures into the proteolytic inner chamber (11). The 19S-RPs-induced radial shifts observed in the β subunits increase the radius of this aperture and may, therefore, serve to make the inner proteolytic sites more accessible to the unfolded substrate proteins. Such rearrangements may contribute to the enhanced proteolytic activity of the 26S proteasome. As in the case of the α rings, one segment of the β rings (β1, β2, β5, β6, and β7) is substantially more displaced than the remaining two subunits (β3 and β4) (Fig. 5, *Biii* and *Ciii*). The observation that this region of the β rings is adjacent to that segment in the α rings showing the largest displacement is an indication of a coordinated effect of the 19S-RP on the whole 20S-CP. In this context it is interesting to note that communication between the β subunit ring and the 19S-RP has previously been suggested on the basis of stabilization of the interaction between 19S-RP and the 20S-CP induced by the inhibitor bortezomid, which binds to the β subunit proteolytic sites (23).

Consequences of Subunit Rearrangement—The overall effect of the subunit rearrangements shown here would be to facilitate substrate entry into the 20S-CP and to enhance its access to the β subunit proteolytic sites. It should be noted that the simple rigid body movements of the α and β subunits used to fit the current maps would alter interactions between the subunits and might, therefore, lead to reduced interaction energy. On the other hand, energy lost in this way may well be compensated by the binding energy of the 19S-RP to the 20S-CP. Furthermore, it is likely that these rigid body movements are accompanied by conformational rearrangements within the subunits which may serve to maintain much of their interaction geometry as seen in the crystal structure of the 20S-CP. Interestingly the magnitude of the subunit displacements found on the 20S-CP upon binding of the 19S-RP is quite similar to those observed in GroEL complexes on ATP hydrolysis (24).

Conclusions—Our three-dimensional structural analysis of the human 26S proteasome shows for the first time that the binding of the 19S-RP itself causes a wide opening of a proteolytic gate in the 20S-CP, required for translocation of unfolded substrates into the proteolytic chamber. We show that the nature of this opening resides mostly in radial displacements of the α subunits of the 20S-CP adjacent to 19S-RPs but also that this may be transmitted further into the 20S-CP structure with the displacement of the β subunits, allowing wider access to the proteolytic sites. The analysis of an asymmetric proteasome complex formed by a 20S-CP associated with a single 19S-RP served as a control to demonstrate that the observed rearrangements were indeed associated with the binding of the regulatory cap, as in such complex the displacement of the 20S-CP subunits, compared with its crystallographic coordinates, are much less evident at the uncapped end of the complex. The new three-dimensional maps of the 26S proteasome presented here also serve as a basis for a preliminary exploration of the organization of some of the 19S-RP subunits.

Acknowledgments—We thank Professor John Squire and Dr. Pradeep Luther for providing access to the JEOL electron microscope. We thank Dr. Paul Sheppard, Biomol International, for valuable discussions.

REFERENCES

1. Goldberg, A. L. (2003) *Nature* **426,** 895–899
2. Löwe, J., Stock, D., Jap, B., Zwickl, P., Baumeister, W., and Huber, R. (1995) *Science* **268,** 533–539
3. Groll, M., Ditzel, L., Lowe, J., Stock, D., Bochtler, M., Bartunik, H. D., and Huber, R. (1997) *Nature* **386,** 463–471
4. Groll, M., Bajorek, M., Köhler, A., Moroder, L., Rubin, D. M., Huber, R., Glickman, M. H., and Finley, D. (2000) *Nat. Struct. Biol.* **7,** 1062–1067
5. Kohler, A., Bajorek, M., Groll, M., Moroder, L., Rubin, D. M., Huber, R., Glickman, M. H., and Finley, D. (2001) *Biochimie* (*Paris*) **83,** 325–332
6. Voges, D., Zwickl, P., and Baumeister, W. (1999) *Annu. Rev. Biochem.* **68,** 1015–1068
7. Ludtke, S. J., Baldwin, P. R., and Chiu, W. (1999) *J. Struct. Biol.* **128,** 82–97
8. van Heel, M., Gowen, B., Matadeen, R., Orlova, E. V., Finn, R., Pape, T., Cohen, D., Stark, H., Schmidt, R., Schatz, M., and Patwardhan, A. (2000) *Q. Rev. Biophys.* **33,** 307–369
9. Frank, J., Radermacher, M., Penczek, P., Zhu, J., Li, Y., Ladjadj, M., and Leith, A. (1996) *J. Struct. Biol.* **116,** 190–199
10. Navaza, J., Lepault, J., Rey, F. A., Alvarez-Rúa, C., and Borge, J. (2002) *Acta Crystallogr. D. Biol. Crystallogr.* **58,** 1820–1825
11. Unno, M., Mizushima, T., Morimoto, Y., Tomisugi, Y., Tanaka, K., Yasuoka, N., and Tsukihara, T. (2002) *Structure* **10,** 609–618
12. Walz, J., Erdmann, A., Kania, M., Typke, D., Koster, A. J., and Baumeister, W. (1998) *J. Struct. Biol.* **121,** 19–29
13. Nickell, S., Beck, F., Korinek, A., Mihalache, O., Baumeister, W., and Plitzko, J. M. (2007) *FEBS Lett.* **581,** 2751–2756
14. Nickell, S., Mihalache, O., Beck, F., Hegerl, R., Korinek, A., and Baumeister, W. (2007) *Biochem. Biophys. Res. Commun.* **353,** 115–120
15. Smith, D. M., Kafri, G., Cheng, Y., Ng, D., Walz, T., and Goldberg, A. L. (2005) *Mol. Cell* **20,** 687–698
16. Smith, D. M., Chang, S.-C., Park, S., Finley, D., Cheng, Y., and Goldberg,

A. L. (2007) *Mol. Cell* **27,** 731–744
17. Bennett-Lovsey, R. M., Herbert, A. D., Sternberg, M. J. E., and Kelley, L. A. (2008) *Proteins* **70,** 611–625
18. Huber, A. H., Nelson, W. J., and Weis, W. I. (1997) *Cell* **90,** 871–882
19. Kajava, A. V. (2002) *J. Biol. Chem.* **277,** 49791–49798
20. Whitby, F. G., Masters, E. I., Kramer, L., Knowlton, J. R., Yao, Y., Wang, C. C., and Hill, C. P. (2000) *Nature* **408,** 115–120
21. Ortega, J., Heymann, J. B., Kajava, A. V., Ustrell, V., Rechsteiner, M., and Steven, A. C. (2005) *J. Mol. Biol.* **346,** 1221–1227
22. Rechsteiner, M., and Hill, C. P. (2005) *Trends Cell Biol.* **15,** 27–33
23. Kleijnen, M. F., Roelofs, J., Park, S., Hathaway, N. A., Glickman, M., King, R. W., and Finley, D. (2007) *Nat. Struct. Mol. Biol.* **14,** 1180–1188
24. Ranson, N. A., Clare, D. K., Farr, G. W., Houldershaw, D., Horwich, A. L., and Saibil, H. R. (2006) *Nat. Struct. Mol. Biol.* **13,** 147–152